Biomass Conversion and Biorefinery
https://doi.org/10.1007/s13399-024-06161-5

ORIGINAL ARTICLE

Preparation and characterization of activated carbon from medlar seed by chemical activation with phosphoric acid and its application in uranium adsorption

Messaoud Bennemla[1] · Toufik Semaoune[1] · Meriem Chabane Sari[1] · Fatima Houhoune[1] · Sihem Khemaissia[1] · Mourad Bellaloui[1] · Hamana Adjedar[1] · Yasmina Hammache[1] · Sihem Ouattas[1]

Received: 28 June 2024 / Revised: 29 August 2024 / Accepted: 11 September 2024

Abstract

The aim of this work was to synthesize a high-capacity adsorbent from medlar seeds by chemical activation using phosphoric acid. The confirmation of successful biomass activation was achieved through various characterizations, including SEM–EDS, FTIR, and nitrogen adsorption–desorption. The best parameters were found to be a temperature of 500 °C, a time of 60 min, and an impregnation ratio of 2:1. The specific surface area, average pore diameter, and total pore volume were identified as 1845.32 m^2/g, 2.88 nm, and 0.896 cm^3/g, respectively. The performance of the selected activated carbon was evaluated by using it for the sorption of uranium (VI) in a batch system. The maximum adsorption of 52.08 mg/g was obtained under optimum conditions: pH = 3.54, adsorbent dose of 2 g/L, adsorbate concentration of 100 mg/L, particle size between 0.125 and 0.20 mm, and contact time of 90 min. Until the fifth cycle of use, the prepared activated carbon showed excellent regeneration capacity (84.23%). The pseudo-second-order kinetic and the Langmuir isotherm were the best fitted, implying the monolayer chemical adsorption process. The adsorption process could be considered as spontaneous ($\Delta G° < 0$) and exothermic process (− 84.601 kJ/mol).

Keywords Uranium · Adsorption · Activated carbon · Chemical activation · Kinetic · Wastewater

1 Introduction

The nuclear industry generates high amounts of contaminated water from various sources that require specific treatments according to their chemical composition [1–3]. Uranium is among the major pollutants in those effluents, and it is not only considered as a toxic heavy metal but also has radioactivity character [4–6]. The accumulation of uranium in the environment causes an irreversible impact on human health [7–9], owing to its long half-life and high toxicity. Therefore, special attention has been given to the effective treatment and control of effluents from the nuclear industry in order to generate the least amount of waste. Many technologies have been attempted to remove uranium from aqueous solutions such as chemical precipitation [10–12], ion exchange [13–15], and membrane separation [16, 17]. Compared with these technologies, the adsorption is considered as a promising method because of its low economic cost, wide range of material sources, high selectivity, and high adsorption efficiency. Therefore, several kinds of adsorbents have been suggested for uranium adsorption, including porous nanomaterials [18–20] and activated carbon [21]. Among them, activated carbons are currently seen as a suitable alternative for heavy metal ion adsorption because of their developed surface area and microporosity, excellent adsorption performance, inexpensive production, and low energy of regeneration [22, 23]. In general, activated carbon is made from different biomasses through physical,

Highlights
- The use of activated carbon has increased due to its high sorption capacity and low cost.
- Activated carbon (AC-500-2) was prepared by chemical activation with phosphoric acid.
- The main properties and characteristics of AC-500-2 sorbent were investigated.
- The adsorption performance of carbon from medlar seed could be significantly improved after chemical activation with H_3PO_4.
- The isotherm models and the kinetic parameters of the uranium adsorption process were estimated.

✉ Messaoud Bennemla
m-bennemla@crnd.dz

[1] Nuclear Research Center of Draria, Bp 43 Sébala-Draria, Algiers, Algeria

Published online: 19 September 2024

chemical, biological [24], and hydrothermal carbonization methods [25]. Chemical activation methods are preferred over physical, biological, and hydrothermal activation due to their lower energy cost, quicker pyrolysis time, increased surface area, and greater yield of activated carbon products. Chemical activation involves both pyrolysis and activation in one continuous process, where fresh biomass is immersed in chemical substances like H_3PO_4 or $ZnCl_2$ and then subjected to thermal decomposition. Chemical activation is quite significant, as modifying the surface through impregnation with suitable eco-friendly chemical substances not only boosts adsorption capacity but also enhances the selectivity of carbon properties [26]. Many substances such as phosphoric acid (H_3PO_4), potassium hydroxide (KOH), and zinc chloride have been used as chemical agents. Phosphoric acid is preferred among chemical activation agents for its ability to effectively create mesopores, leading to increased total pore volume and diameter [27]. Activated carbon can be obtained from any low-cost material with a high carbon content and low inorganic content, such as olive bagasse, sugarcane bagasse, rice-husk soybean straw, potato peel, and other lignocellulosic materials [28–30]. Medlar seeds are another solid waste with great potential for the synthesis of activated carbon. Brown or occasionally reddish-purple, the medlar seed is a fruit with a variety of dimensions (0.5 to 2.5 cm). Medlar trees are widely grown in China, which is the world's leading producer. It is relatively widespread in Japan, Spain, Turkey, and Algeria, where it plays an important role in the rural economy [31]. Therefore, large quantities of medlar seeds are produced every year [32]. Medlar seeds are considered food waste and are regularly disposed of in landfills, which has a negative impact on the environment. Thus, the development of a sustainable alternative for the conversion of this waste into a useful resource would be highly beneficial [33].

In this study, in order to increase the uranium (VI) adsorption efficiency, activated carbon based on medlar seeds was prepared by chemical activation using phosphoric acid and high-temperature carbonization. The resulting materials were characterized by means of SEM, EDS, FTIR, PZC, and nitrogen adsorption–desorption. Various parameters affecting the adsorption process such as initial pH, reaction time, particle size, adsorbent dose, and initial concentration of uranium (VI) were investigated and optimized. In addition, the isotherm, kinetic, and thermodynamic properties of U(VI) adsorption by activated carbon were also investigated.

2 Material and methods

2.1 Chemicals and materials

The medlar seeds used in this study were supplied from a small local factory. Uranium nitrate ($UO_2(NO_3)_2{\cdot}6H_2O$, 99%), arsenazo III ($C_{22}H_{18}As_2N_4O_{14}S_2$, > 99%), and nitric acid (HNO_3, 63%) were purchased from Merck. Phosphoric acid (H_3PO_4, 85%) was supplied by BDH Prolabo. Potassium nitrate (KNO_3, 99%) and sodium hydroxide (NaOH, 98%) were obtained from Aldrich. The amount (2.11 g) of uranium nitrate ($UO_2(NO_3)_2{\cdot}6H_2O$) was dissolved in 1000 ml of distilled water to prepare uranium stock solution (1 g/L). A small amount of concentrated nitric acid was added to the uranium solution to avoid hydrolysis. The desired concentration of U(VI) solutions was obtained by an appropriate dilution of the stock solution with distilled water. The pH value of the solution was adjusted by adding a few drops of sodium hydroxide (0.1 M) or nitric acid (0.1 M) to the U(VI) ion solution. All reagents used in this study were of analytical grade.

2.2 Synthesis of activated carbon

In this study, the medlar seeds were used as the starting material for the preparation of activated carbon. Activated carbon was synthesized by the chemical activation of the dried medlar seed powder using H_3PO_4 as a chemical agent. After separating the medlar seeds from the pulp, the seeds were washed several times with boiling water to remove impurities until clear washing water was obtained. The washed material was dried in an oven at 105 °C for 24 h. The medlar seeds were ground and sieved into four different particle sizes: 0.125–0.20, 0.20–0.50, 0.5–0.70, and > 0.70 mm. The obtained fractions were washed with distilled water to remove dust and impurities and then dried at 105 °C for 48 h. The dried medlar seed powders produced were impregnated with a concentrated solution of H_3PO_4 at 40 wt.% in the ratios (IR) of 1:1, 2:1, and 3:1, calculated as the ratio of H_3PO_4 weight in solution to the weight of the dried medlar seed powder using Eq. (1). Impregnated samples were then activated in a muffle furnace at 400 °C, 500 °C, 600 °C, and 700 °C under a nitrogen flow rate of 50 ml/min for 60 min. Then, the activated carbons were allowed to cool down to room temperature. They were then thoroughly rinsed with distilled water to ensure the complete removal of any remaining activation agent (pH between 5 and 6). Finally, the washed materials were dried in an oven at 105 °C for 24 h and stored in a desiccator for future use.

$$\mathrm{IR}_{=W_{\mathrm{H3PO4}}/W_P} \quad (1)$$

2.3 Characterization

The morphology of the activated carbon was observed by scanning electron microscopy analysis (SEM, JEOL JSM-7610F Plus), and the elemental composition was analyzed by energy dispersive analysis, using a Bruker X-Flash EDS

detector. EDS acquisition was conducted on three different sections of the material. Fourier Transform Infrared Spectroscopy (FTIR) spectra analysis (JASCO FT-IR-460 PLUS) was used to identify the functional groups on the surface of the activated carbon. The nitrogen adsorption–desorption isotherms at 77 K were performed using a Micromeritics ASAP 2010 surface area analyzer. The specific surface area, micropore volume, and micropore surface area of the activated carbon were analyzed using the Brunner, Emmet, and Taylor (BET) method. The Laser Particle Size MASTERSIZER HYDRO 2000 S (MALVERN) was used to obtain accurate and detailed particle size distributions. Uranium (IV) concentration was determined before and after equilibrium using a UV–vis spectrophotometer (SAFS monaco UVmc[1]). The pH of the solutions was measured using a HANNA HI5221-02 pH meter. The ash contents of the dried medlar seed powder and the synthesized activated carbons were determined in accordance with the ASTM D2866-11 standard method, and the activated carbon yield (Y_{AC}) was calculated using Eq. (2).

$$Y_{AC=W_{AC}/W_P} \tag{2}$$

where W_{AC} is the weight of the dried activated carbon and W_P is the weight of the medlar seed powder.

The point of zero charge of sample was determined by pH drift method [34]. A sample weighing 0.1 g was introduced into 20 ml of 0.01 M KNO_3, and the pH was adjusted to different levels (from 1 to 10) using KOH or HNO_3. The samples were stirred at a rate of 300 rpm for 48 h at room temperature. Once equilibrium was reached, the solutions were centrifuged, and the final pH of each solution was measured with a pH meter. A graph plotting pH_i against pH_f can be created, where pH_i represents the initial pH and pH_f represents the final pH of the solution. The pH value at the intersection of the bisector and the pH_i-pH_f curve is identified as the pH_{PZC} value.

2.4 Adsorption experiments

The uranium (VI) sorption behavior of AC-500–2 was performed under stirring (300 rpm) in Erlenmeyer flasks containing known amounts of sorbent (50, 80, 100, and 150 mg) with 50 ml of uranium solutions at room temperature (298 K) and a predetermined pH. The effects of initial pH of the solution, contact time, sorbent weight, particle size, and initial uranium ion concentration were studied in order to optimize the adsorption process. After reaching the equilibrium, the adsorbents were separated from the uranium solution by centrifugation and the residual uranium was determined using a UV–vis spectrometer at 664 nm with Arsenazo III as complexing agent. All the experiments were performed in duplicate, and the average value was used in all cases. The uranium (VI) adsorption efficiency R (%), adsorption capacity q_t (mg/g), and distribution coefficient K_d (L/g) were calculated by Eqs. (3), (4), and (5), respectively.

$$R(\%) = 100 * (C_0 - C_e)/C_0 \tag{3}$$

$$q_e = \left(C_0 - C_t\right) * V/m \tag{4}$$

$$K_d = \left(\left(C_0 - C_e\right)/C_e\right) * (V/m) \tag{3}$$

where C_0 and C_e are the initial and equilibrium U(VI) concentration in mg/L, respectively. C_t (mg/L) is the concentration of U(VI) at time t, and V/m is the ratio of the volume of the U(VI) solution (ml) to the amount of sorbent (g).

3 Results and discussion

3.1 Characterization of the activated carbon

3.1.1 N_2 adsorption–desorption isotherm

The porosity and specific surface area of the activated carbons (ACs) prepared at different temperatures (400, 500, 600, and 700 °C) were analyzed through N_2 adsorption–desorption methods. As illustrated in Fig. 1, all the isotherms exhibited the same profile with horizontal plateaus at higher relative pressures. According to the IUPAC classification, these isotherms belong to the type IV class [35]. The nitrogen adsorption capacity increased rapidly in the relative pressure range of 0–0.20, which may be due to the fact that nitrogen molecules speedily fill the micropore structures [36]. The small branch of hysteresis indicated

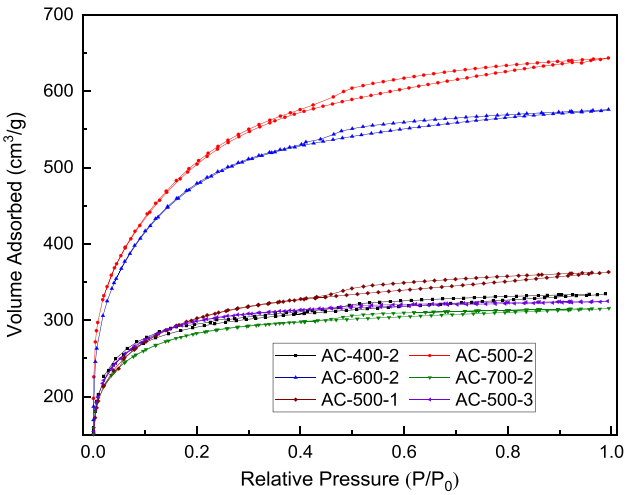

Fig. 1 N_2 adsorption–desorption isotherms of activated carbons produced at different temperatures

that the activated carbon consists of mainly of micropores accompanied by few mesopores [37]. After complete filling of the micropores, the presence of some mesopores leads to a gradual increase in adsorption [38].

The effects of temperature treatment on the pore characteristics of activated carbons are shown in Table 1. It can be observed that the specific surface area and the total pore volume of the ACs increase significantly with the increase of the activation temperatures from 400 to 500 °C. When the activation temperature was further increased from 500 to 700 °C, the BET surface area decreased from 1845.32 to 1034.58 m^2/g and the total pore volume decreased from 0.896 to 0.48 cm^3/g. According to previous work, the low specific surface area observed at 400 °C is mainly due to the many carbon atoms and phosphoric acid that could not absorb enough energy to participate in a pore formation reaction at this temperature [39]. The BET surface area of the current activated carbon is comparable to the value reported for palm husk (2000 m^2/g) [40] and exceeds those reported for grape seed [41], durian husk [42], pumpkin seed husk [43], coconut husk [44], cashew nut husk [45], date palm husk [46], and castor seed husk [47], listed in Table 2. Raising the activation temperature results in the extension of micropores and the creation of additional mesopores and macropores. However, if pores widen too much and their walls thin too much, it may cause them to collapse, resulting in a reduction of micropore and BET surface areas [48]. Furthermore, raising the activation temperature decreases the activated carbon yield because it leads to lignin combustion in the biomass and the release of additional volatile compounds [49]. The surface area and pore volume of activated carbons increased also as the phosphorus/carbon ratio increased from 1:1 to 2:1; however, there was a significant decrease in both of these parameters as the ratio increased from 2:1 to 3:1. Therefore, it was recommended to maintain a phosphorus/carbon ratio of 2:1 to achieve effective activation with minimal phosphorus consumption. As a result, AC-500–2 was chosen as the best activated carbon due to its good surface area and pore volume and was used in the adsorption experiments.

3.1.2 SEM analysis

Figure 2 shows the morphology and texture of the surface of the selected activated carbon AC-500–2 by scanning electron microscopy (SEM). As can be seen, the activated carbon produced has an orderly and extremely porous structure. Different pore sizes can be observed. The pores are not perfectly spherical, the porous structures did not continue inward, and the pores were not connected to each other. As

Table 1 Textural characteristics of medlar seed powder treated with H_3PO_4 at various impregnation ratios and temperatures for 60 min

Samples	T °C	IR	Ash (%)	Yield (%)	S_{BET} (m^2/g)	S_{micro} (m^2/g)	V_{micro} [(a)] (cm^3/g)	V_{meso} [(a)] (cm^3/g)	V_T (cm^3/g)	Pore diameter (nm)
AC-400–2	400	2:1	0.54	56.85	1082.79	699.84	0.280	0.234	0.514	3.19
AC-500–2	500	2:1	0.87	44.26	1845.32	446.57	0.162	0.734	0.896	2.88
AC-600–2	600	2:1	1.18	43.19	1765.46	609.03	0.225	0.594	0.819	2.68
AC-700–2	700	2:1	2.41	39.75	1034.58	669.39	0.274	0.206	0.48	2.76
AC-500–1	500	1:1	1.21	41.79	1091.89	519.99	0.212	0.498	0.710	3.10
AC-500–3	500	3:1	1.56	46.73	1427.63	78.24	0.0065	0.610	0.616	3.97

[(a)]The specific surface area calculated using the BET method; micropore volume determined by BJH method

Table 2 BET surface area and yield of activated carbon from different precursor materials using H_3PO_4 activation agent

Precursor	Activation parameters			Surface area (m^2/g)	Yield (%)	References
	T (°C)	Time (min.)	IR			
Medlar seeds	500	60	2:1	1845.32	43.62	This work
Grape seed	500	120	1:3	1139	50	[41]
Durian shell	500	20	30 wt.%	1404	-	[42]
Pumpkin seed shell	500	60	2:1	1421	31	[43]
Coconut shell	600	120	1:1	479.17	-	[44]
Cashew nut shells	600	120	1.7:1	1514	85	[45]
Palm shell	475	75	1.75:1	2000	44–55	[40]
Date palm bark	400	180	40 wt.%	902	30	[46]
castor seed hull	700	60	0.8:1	785.38	78.86	[47]

mentioned in the literature, H_3PO_4 biomass treatment techniques start with cellulose depolymerization and then move on to biopolymer dehydration, aromatic ring formation, and finally, the release of phosphate clusters that allow the formation of new pores and the expansion of existing pores on the activated carbon surface [50–52]. Moreover, increasing the activation temperature also enhances the number of narrow micropores and expands the existing micropores through the use of activating agents, as a result of the melting of compounds present in biomass [53]. This claim has been supported by the majority of previous studies documented in their research papers.

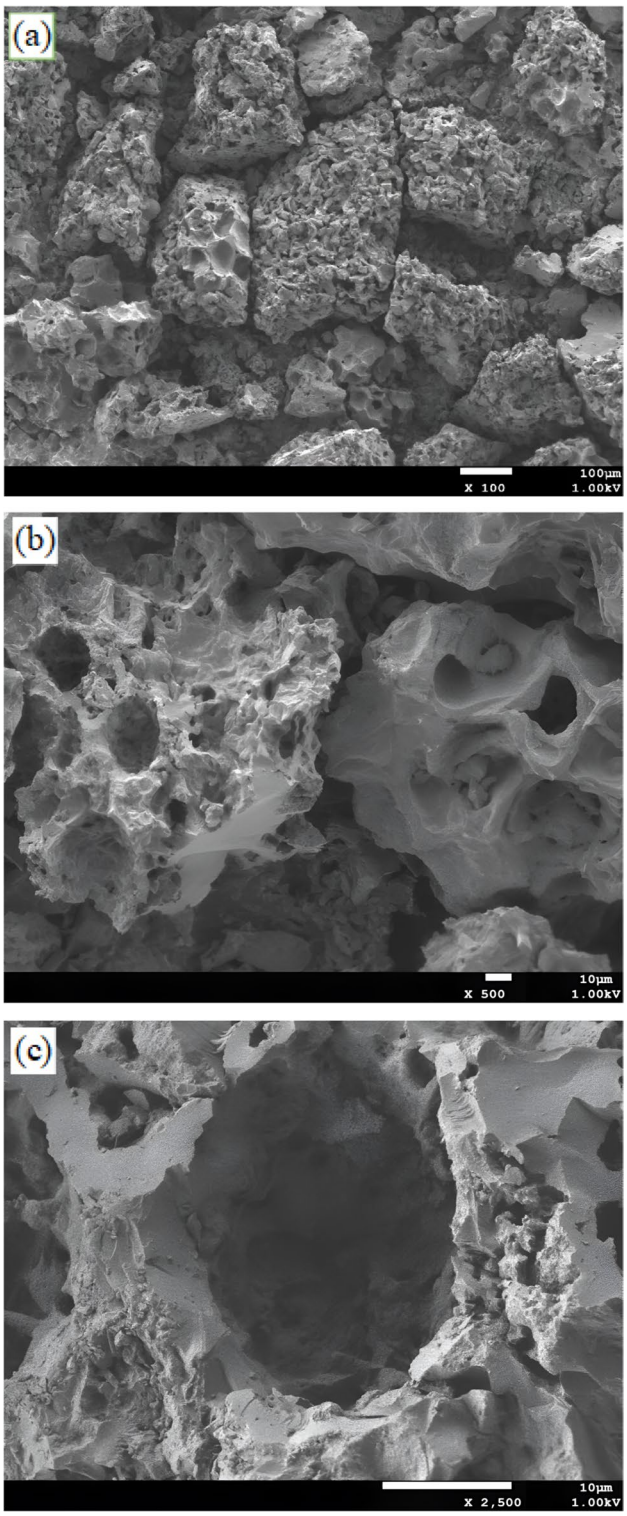

Fig. 2 SEM micrographs of AC-500–2 sample: **a** 100x, **b** 500x, and **c** 2500

3.1.3 Elemental analysis

The elemental analysis of the medlar seeds and the resulting activated carbon samples are shown in Table 3. As can be seen, carbon and oxygen are the dominant atoms in all samples. The biomass carbon content was 44.70%, and the activated carbon values were 57.50%, 86.42%, 85.802%, and 85.34% for AC-400–2, AC-500–2, AC-600–2, and AC-700–2, respectively, while the amount of oxygen, hydrogen, and nitrogen decreased due to the partial decomposition of volatile compounds and degradation of organic substances at high temperatures [54]. Increased carbon content in biomass is indicative of a high-quality precursor that will deliver the best possible amount of activated carbon [55]. Furthermore, the biomass sample contains almost no phosphor, but the AC samples contain approximately 4.50% phosphor. This finding suggests that phosphorus doping in the precursor sample is remarkably effective [56].

3.1.4 Functional group analysis

Figure 3 shows the FTIR spectra of activated carbons prepared from medlar seeds by phosphoric acid activation at different impregnation ratios and activation temperatures (400, 500, 600, and 700 °C). As can be seen, the FTIR spectra of the activated carbons show a number of changes as the activation temperature is increased from 400 to 700 °C. The broadband between 3600 and 3300 cm^{-1} in the spectrum of all samples corresponds to hydroxyl and carboxyl groups [57, 58]. The presence of two characteristic bands for the C-H bonds of alkyl groups between 2827 and 2970

Table 3 Elemental analysis of medlar seed and ACs

(wt.%)	Carbon	Hydrogen	Nitrogen	Oxygen	Phosphor
Precursor	43.70	7.22	1.46	47.58	0.027
AC-400–2	77.50	3.25	1.28	12.61	5.34
AC-500–2	86.42	1.18	0.74	7.19	4.43
AC-600–2	85.80	2.13	0.716	7.124	4.22
AC-700–2	85.34	3.16	0.64	6.471	4.28
AC-500–1	85.743	1.84	1.14	8.48	2.74
AC-500–3	83.26	1.42	0.86	8.71	5.73

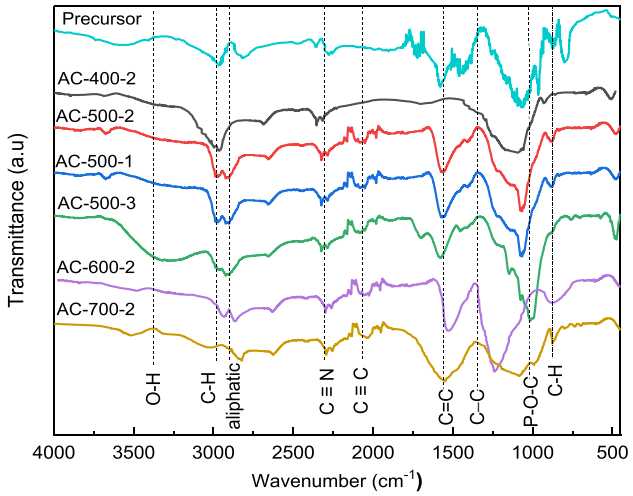

Fig. 3 FTIR spectrum of dried medlar seed powder and prepared activated carbons

cm^{-1} indicates the presence of aliphatic groups [59], whose intensity decreases with increasing activation temperature [60]. The adsorption band observed around 2324 cm^{-1} can be attributed to the stretching vibration of C≡N, while the peak located at 2068 cm^{-1} has been assigned to the stretching vibrations of C≡C alkyne groups [61]. The band at about 1563 cm^{-1} can be attributed to the stretching vibration of C = C [62]. Similarly, the adsorption band located at 1415 cm^{-1} belongs to the C–C stretching vibration in the aromatic rings [60]. The band observed at about 110 cm^{-1} in all samples belongs to the stretching vibrations of the following phosphorus species: hydrogen-bonded P = O groups from phosphates or polyphosphate chains, the O-C stretching vibration in the P-O-C aromatics, and P = OOH [58, 63]; however, the density of this band decreases with increasing activation temperature. As the impregnation rate increases from 1 to 3, the relative intensity of the band at 1100 cm^{-1} increases, indicating the presence of more phosphorus-containing groups [64]. Finally, a band appeared at 882 cm^{-1}, which was correlated to unsaturated C-H out-of-plane bending vibration [65].

3.1.5 Point of zero charge

The results for pH_{PZC} are illustrated in Fig. 4. The pH curves indicating the point of zero charge show that the dried medlar seed powder has a neutral pH value of 6.54, whereas the activated carbon sample AC-500–2 exhibits an acidic nature with a pH_{PZC} of 3.45. When comparing the pH_{PZC} of the original material, it is evident that the activation process leads to a reduction in the point of zero charge [66]. This acidic characteristic aligns with expectations, as the activation of the carbon was conducted using phosphoric acid [67]. The surface of activated carbon exhibits a positive charge when the pH is below 3.54, due to the protonation of phosphate groups. However, as the pH increases, the surface charge becomes less positive. This is because, at higher pH values, the phosphate groups undergo deprotonation and dissociation, leading to an increase in the number of negatively charged ions on the surface [68]. When the pH exceeds 3.54, the surface acquires a negative charge, which enhances the adsorption of cations [66].

3.2 Adsorption studies

3.2.1 Effect of pH

The surface charge of the activated carbon and the species distribution of uranium can be affected by the pH of the solution, which can further affect the adsorption of uranium on the activated carbon [69, 70]. The effect of pH on the adsorption of uranium (VI) on AC-500–2 was carried out in the pH range of 1.0–5.0, and the results are shown in Fig. 5. As can be seen, at pH = 1.0, the adsorption capacity of AC-500–2 was the lowest (22.25 mg/g). With the increase of pH value, the uranium adsorption capacity of AC-500–2 gradually increased and reached the maximum value of 49.84 mg/g at pH 3.54. Then, the adsorption capacity of AC-500–2 started to decrease with the further increase of pH. These findings indicate that the pH level of the solution plays an important role in the adsorption of U(VI).

The low adsorption in the acidic range could be explained by the protonation of functional groups of activated carbon surface, which reduces their capacity to bind positively charged UO_2^{2+} ions [71]. As the pH increased from 1.0 to 3.0, the number of protons present in the solution decreased and the electrostatic repulsion between activated

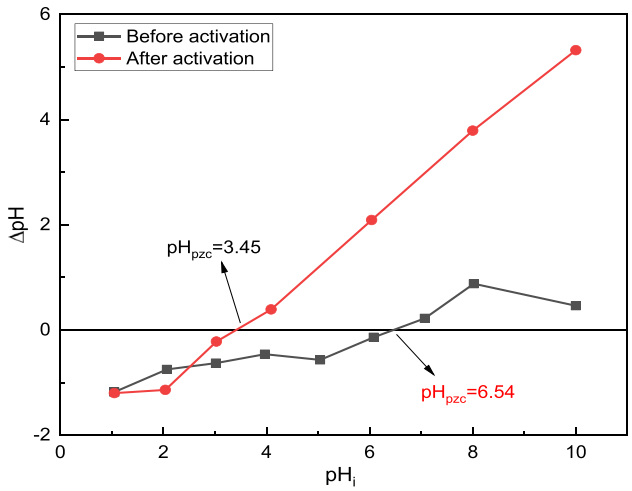

Fig. 4 Determination of the point of zero charge (pHpzc) for both dried medlar seed powder and the selected activated carbon AC-500–2

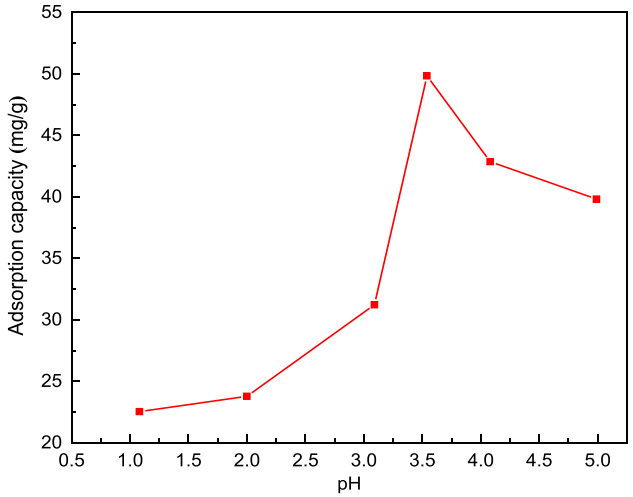

Fig. 5 Effect of pH value on uranium (VI) adsorption by activated carbon AC-500–2 (C_0 = 100 mg/L, contact time 90 min, adsorbent dose 2 g/L, particle size 0.125–25 mm, agitation speed 300 rpm, and T = 25 °C)

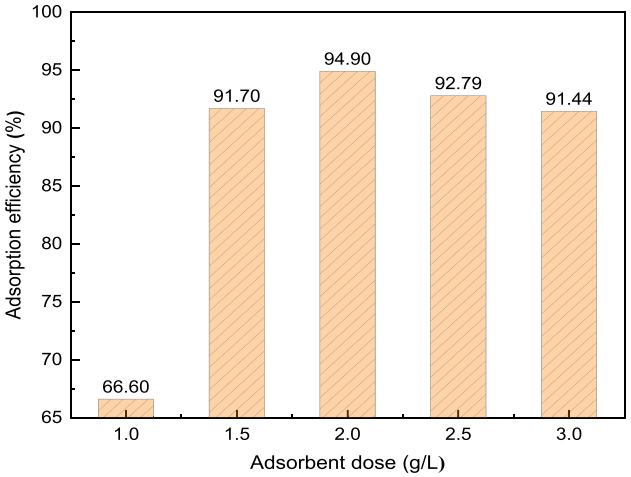

Fig. 6 Effect of adsorbent dose of AC-500–2 on uranium adsorption. Contact time 90 min, initial pH 3.54, initial uranium concentration 100 mg/L, particle size 0.125–0.20 mm, agitation speed 300 rpm, and T 25 °C

carbon and positively charged uranium species (UO_2^{2+}) was weakened by deprotonation of the functional groups, resulting in slightly increased uranium removal from 22.55 to 31.23 mg/g. At pH = 3.54, above the point of zero charge, the surface of the activated carbon becomes negatively charged, while the uranium is mainly in the form of UO_2^{2+} [71, 72]. Therefore, there is a strong electrostatic attraction between them, which improves the adsorption efficiency. With further increase of the pH value from 3.54 to 5, the adsorption capacity decreased from 49.84 to 39.82 mg/g, which might be caused by the transformation of uranium species from cations (UO_2^{2+}) to hydrated uranium complex species ($((UO_2)_2(OH)_2^{2+}$ and $(UO_2)_3(OH)^{5+}$) [70, 72], which are difficult to be captured by active sites. Therefore, pH = 3.54 is suggested as the best pH value for further sorption experiments. During the experiment, it was observed that when the pH is higher than 5, the uranyl ions in the solution would precipitate. Thus, only the effect of the pH value between 1 and 5 was investigated.

3.2.2 Effect of adsorbent dose

The relation between the adsorbent dose and the adsorption efficiency was carried out in de range of 1 to 3 g/L, and the results are shown in Fig. 6. As can be seen, the adsorption efficiency of uranium (VI) increases with the increase of adsorbent dosage and reaches the maximum (94.89%) at the adsorbent dose of 2.0 g/L, after which the adsorption efficiency decreases slightly (91.43%). The increasing trend may be due to an increase in the number of adsorption sites and the contact probability between UO_2^{2+} ions and the available adsorption sites [73]. However, the decreasing trend can be explained by the greater number of active sites of the adsorbent in aqueous solution compared to the number of uranium ions, thus leaving many active sites unused [74]. Therefore, the adsorbent dose of 2.0 g/L was considered as the optimal and selected for all further experiments.

3.2.3 Effect of initial concentration

The effect of the initial uranium concentration was investigated by using seven different uranium solutions varying in the range of 20–200 mg/L, and the results are shown in Fig. 7. It can be seen that the adsorption capacity of uranium (VI) increases from 9.67 to 52.08 mg/g with the increase of initial uranium concentration from 20 to 200 mg/L, while the adsorption efficiency of uranium (VI) decreases from 96.20 to 58.8%. The higher adsorption efficiency obtained at lower concentration may be due to the presence of a large number of free adsorption sites on the surface of the adsorbent available to combine with uranyl ions. As the concentration increases, the number of uranyl ions in solution increases, while the number of the adsorption sites on the surface of the adsorbent remains constant; thus, the active sites of the adsorbent are gradually saturated, resulting in a decrease in the adsorption efficiency of uranyl ions (UO_2^{2+}) [75]; however, as the concentration increased, more uranyl ions were adsorbed compared to low initial concentrations, which may be due to the enhancement of the driving force between uranyl ions and functional groups on the surface of the adsorbent during the adsorption process [76].

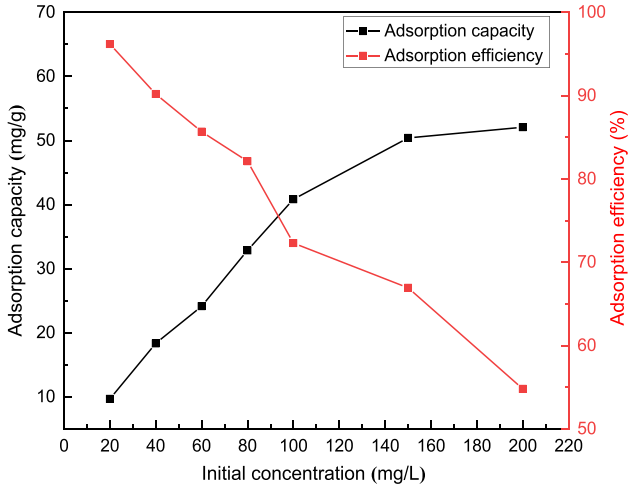

Fig. 7 Effect of initial concentration on the adsorption capacity and adsorption efficiency of U(VI) onto AC-500–2, pH 3.54, adsorbent dose 2 g/L, particle size 0.125–0.20 mm, contact time 90 min, agitation speed 300 rpm, and T 25 °C

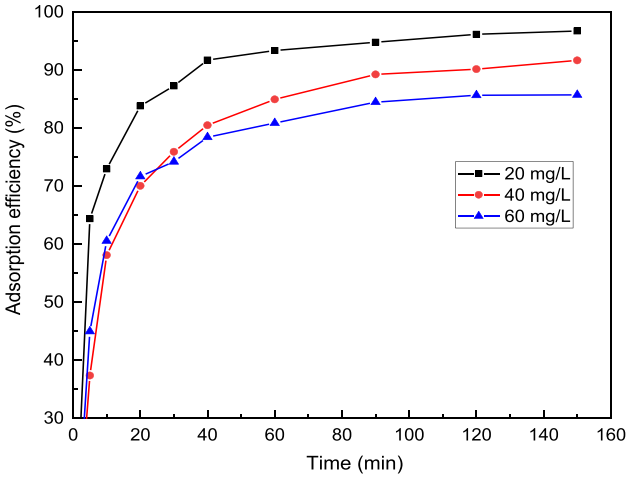

Fig. 8 Effect of contact time on the adsorption of uranium (VI) onto AC-500–2; pH 3.54, adsorbent dose 2 g/L, particle size 0.125–0.20 mm, agitation speed 300 rpm, and T 25 °C

3.2.4 Effect of contact time

Figure 8 describes the adsorption of uranium (VI) on AC-500–2 at various concentrations in the time range of 5 from 180 min. The adsorption process carbon can be divided into three phases. During the first 20 min, the adsorption of uranium increased rapidly and then slowed down slightly until the adsorbents reached saturation within 90 min. When the contact time exceeded 90 min, the adsorption percentage remained almost the same. The increasing trend in the initial stage can be ascribed to the availability of a large number of empty adsorption sites on the surface of the adsorbent [77]. However, when many active sites were occupied, the adsorption efficiency of uranyl ions (UO_2^{2+}) gradually decreased, and the adsorption tended to reach equilibrium, and finally, the saturation [77]. Moreover, the increased adsorption efficiency at longer contact times can also be attributed to a reduction in the resistance of the boundary layer surrounding the sorbent particles to mass transfer [78].

3.2.5 Effect of particle size

The effect of particle size of AC-500–2 on the adsorption of uranium was investigated at four particle sizes of 0.125–0.20, 0.20–0.50, 0.50–0.70, and > 0.7 mm, with a fixed concentration of uranium solution (100 mg/L). The result is shown in Fig. 9. It is obvious that both the adsorption efficiency and adsorption capacity are inversely related to the particle size. The adsorption efficiency decreases from 95 to 73.31% when the particle size is increased from 0.125 to 0.2 mm to more than 0.7 mm. This can be attributed to the fact that the smaller particles have a higher specific surface area and a large number of free adsorption sites [79]. Moreover, the increase in the specific surface area improves the interaction between the finer activated carbon particles and the uranyl ions, resulting in a higher adsorption capacity. Thus, the 0.125–0.20 mm particle size was selected for all further adsorption experiments.

3.3 Adsorption kinetics

In order to understand the adsorption mechanism better, the adsorption data were fitted with pseudo-first-order and pseudo-second-order models. These two models can be expressed by the following equations:

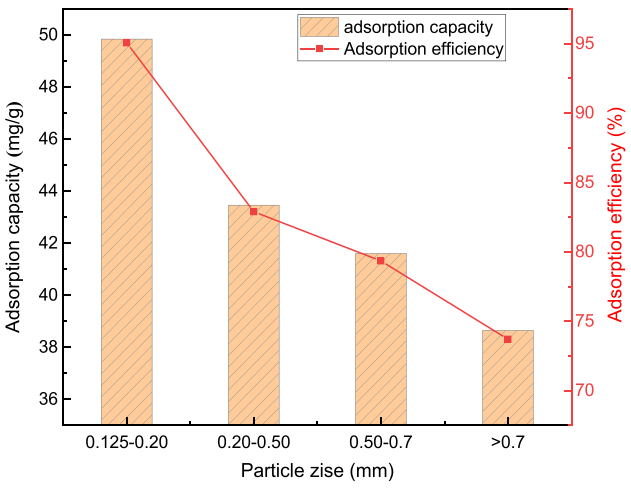

Fig. 9 The effect of particle size on the uranium adsorption onto CA-500–2; C_0 100 mg/L, pH 3.54, adsorbent dose 2 g/L, contact time 90 min, agitation speed 300 rpm, and T 25 °C

$$\text{Pseudo}-\text{first}-\text{order}: \log(q_e - q_t) = \log q_e - \left(K_1 * t/2.303\right) \quad (6)$$

$$\text{Pseudo}-\text{second}-\text{order}: t/q_t = t/q_e + 1/(K_2 * q_e^2) \quad (7)$$

where q_t and q_e are the amounts adsorbed at time t (min) and equilibrium (mg/g), K_1 (min^{-1}) and K_2 (g/mg min) are pseudo-first-order and pseudo-second-order adsorption rate constants, respectively.

The fitting curves and their corresponding parameters are presented in Fig. 10 and Table 4. The results from the kinetic modeling of adsorption indicate that the correlation coefficient R^2 values are nearly equal to one for the second-order model, whereas they are significantly lower for the first-order model. Additionally, the q_e values calculated from pseudo-second order are closer to the experimental data. This leads us to conclude that the adsorption kinetics of U(VI) follows the pseudo-second-order model. However, the results suggested that the ongoing sorption process could be considered as chemisorption, where valence forces are involved in the sharing or exchange of electrons between U(VI) ions and functional groups on the activated carbon surface [80].

3.4 Adsorption isotherms

The adsorption isotherm experiments were carried out on the selected activated material under optimal adsorption conditions, which included an initial pH of 3.54, an adsorbent dosage of 2.0 g/L, a contact time of 90 min, and an agitation speed of 300 rpm at room temperature. The initial concentrations of the uranium solution varied from 20 to 200 mg/L. The experimental data collected were analyzed using the Langmuir and Freundlich models, which are represented by Eqs. (8) and (10), respectively.

$$C_e/q_e = 1/(K_L * q_m) + C_e/q_m \quad (8)$$

$$R_L = 1/(1 + K_L * C_0) \quad (9)$$

$$\log(q_e) = \log(K_F) + (1/n)\log(C_e) \quad (10)$$

where C_e is the equilibrium concentration in mg/L; q_e (mg/g) and q_m (mg/g) are the amount of uranyl ions adsorbed and the maximum adsorption capacity, respectively; K_L (L/mg) and K_F (L/mg) are the Langmuir and Freundlich adsorption equilibrium constants, respectively; n is the intensity of adsorption; R_L is the Langmuir separation factor.

Figures 11 and 12 and Table 5 show the plots and parameters derived from d Langmuir and Freundlich isotherms using experimental data. The data indicates that the linear graphs derived from the two isotherms demonstrate a better alignment of the experimental data with

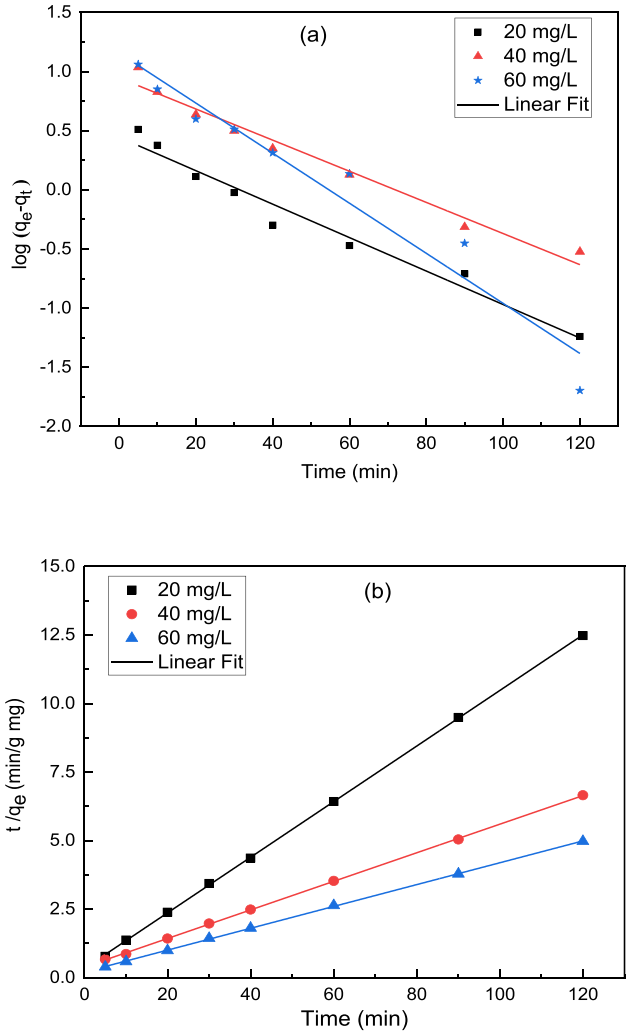

Fig. 10 Plots of kinetic models for the adsorption of uranium (VI) on AC-500–2: **a** pseudo-first-order model and **b** pseudo-second-order model

the corresponding isotherms. The correlation coefficients indicate that the experimental data fitted the Langmuir model ($R^2 = 0.9908$) better than the Freundlich model ($R^2 = 0.986$), suggesting monolayer adsorption on activated carbon surface [81]. K_L and q_m were found to be 0.1295 L/mg and 55.5 mg/g, respectively. Furthermore, the value of R_L obtained from the Langmuir model was less than 1, which confirmed that the U(VI) adsorption process by AC-500–2 was favorable [82]. The adsorption capacity recorded for U(VI) on AC-500–2 was evaluated against other adsorbents found in the literature [83–87], as shown in Table 6. In all the cases mentioned, activated carbon derived from medlar seeds demonstrates superior performance for U(VI) when compared to previous precursor.

Table 4 Kinetic parameters of uranium (VI) sorption onto AC-500–2

C_0 (mg/L)	Pseudo-first-order model			Pseudo-second-order model			$q_{e\ (experimental)}$
	q_e (mg/g)	K_1 (min^{-1})	R^2	q_e (mg/g)	K_2 (g/mg min)	R^2	(mg/L)
20	2.783	0.0325	0.9670	8.673	0.0394	0.9999	9.677
40	8.837	0.0303	0.9742	19.190	0.0070	0.9998	18.339
60	14.346	0.0487	0.9434	25.113	0.0076	0.9998	24.153

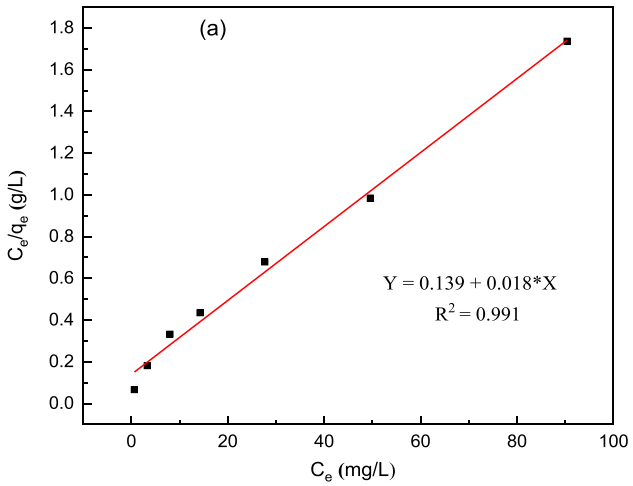

Fig. 11 Langmuir isotherm for uranium (VI) sorption onto AC-500–2

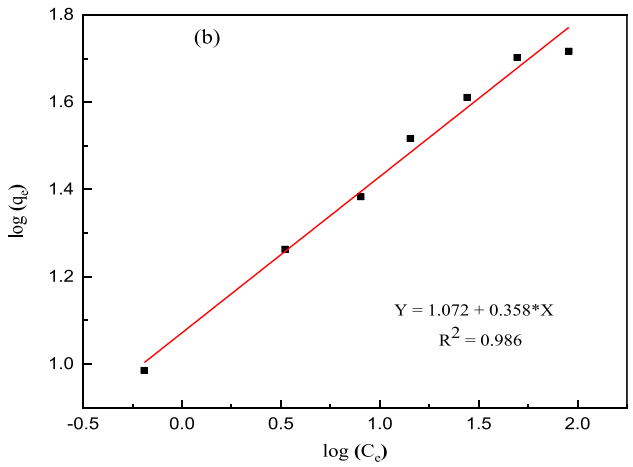

Fig. 12 Freundlich isotherm for uranium (VI) sorption onto AC-500–2

Table 5 The results of Langmuir and Freundlich isotherm parameters

Type of isotherm model	Parameters	Values
Langmuir	R^2	0.991
	K_L (L/mg)	0.129
	q_m (mg/g)	55.5
Freundlich	R^2	0.986
	K_F (L/mg)	11.8
	n	2.793

3.5 Adsorption thermodynamics

Thermodynamic parameters such as standard enthalpy change ($\Delta H°$), standard entropy change ($\Delta S°$), and Gibbs free energy change ($\Delta G°$) are calculated from the Van't Hoff Eq. (11):

$$\mathrm{Ln}K_d = -\frac{\Delta H^0}{\mathrm{RT}} + \frac{\Delta S^0}{R} \tag{11}$$

The Gibbs free energy change ($\Delta G°$) is related to $\Delta H°$ and $\Delta S°$ by the following Eq. (12):

$$\Delta G^0 = \Delta H^0 - T\Delta S^0 \tag{12}$$

where k_d is the distribution coefficient (L/g), T is the temperature (K), R is the universal gas constant (8.314 J/mol K), $\Delta H°$ is the standard enthalpy (kJ/mol), $\Delta S°$ is the standard entropy (kJ/mol K), and $\Delta G°$ is the Gibbs free energy change (kJ/mol).

The values of $\Delta H°$ and $\Delta S°$ can be determined from the slope and intercept of the graph plotted between Ln k_d and $1/T$ (Fig. 13) using Van't Hoff Eq. (11) and $\Delta G°$ can be calculated directly from Eq. (12). The thermodynamic parameters for U(VI) adsorption by AC-500–2 are listed in Table 7. The negative value of $\Delta G°$ indicates spontaneous U(VI) adsorption behavior of AC-500–2 [88]. In addition, increasing values of $\Delta G°$ with increasing temperature suggest a more favorable sorption process at low temperatures. The negative value of $\Delta H°$ (−84.601 kJ/mol) suggested that the sorption of U(VI) on the AC-500–2 was an endothermic process. Also, the negative value of $\Delta S°$ (−0.244 kJ/mol) indicates reduced randomness at the solid–liquid interface during the adsorption process [89].

3.6 Reusability of the adsorbent

Reusability tests of AC-500–2 after U(VI) adsorption were performed in five consecutive cycles with a 0.1 mol/L HNO_3 solution for 3 h, and the results are shown in Fig. 14. The efficiency of 84.23% was obtained after five adsorption–desorption cycles, confirming its excellent regeneration. The maximum adsorption was achieved in the first cycle (95.104%). The adsorption capacities of the other adsorption cycles showed a slight decrease. Due to the fully

Table 6 Comparing U(VI) adsorption capacity on different adsorbents

Precursor	q_{max} (mg/g)	References
Medlar seeds	55.50	This study
AC/PN (activated carbon/polyacrylonitrile)	28.45	[83]
Modified rice stem	1.89	[84]
Olive stones	49.70 (0.171 mmol/g)	[85]
AO-AC (amidoxime/activated carbon)	35.18	[86]
Areca residue	2.27	[87]

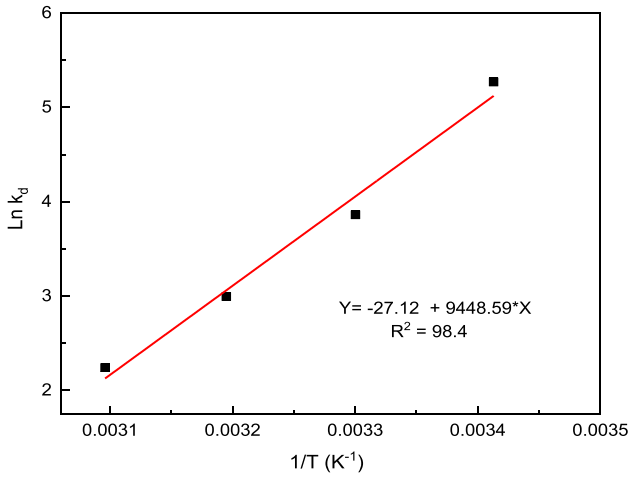

Fig. 13 Plot of Ln (k_d) vs. 1/T for U(VI) adsorption on AC-500–2

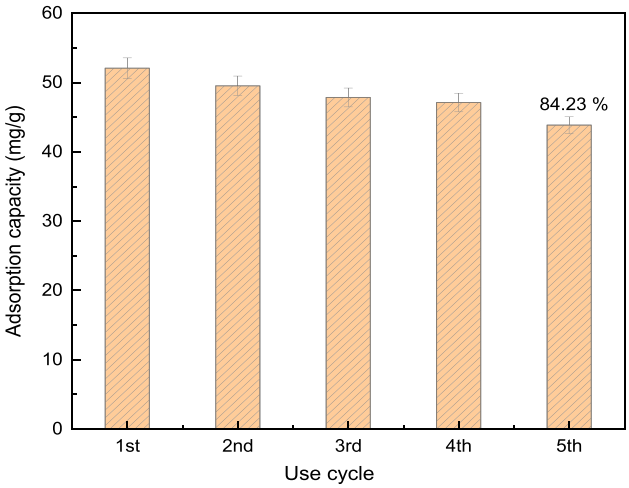

Fig. 14 The sorption capacity of U(VI) by AC-500–2 at five regeneration cycles. C_0 100 mg/L, pH 3.54, adsorbent dose 2 g/L, contact time 90 min, agitation speed 350 rpm, and T 25 °C

Table 7 Thermodynamic parameters for U(VI) adsorption

T (K)	$\Delta H°$ (kJ/mol)	$\Delta S°$ (kJ/mol K)	$\Delta G°$ (kJ/mol)
293	− 84.601	− 0.244	− 12.862
303			− 10.413
313			− 7.965
323			− 5.517

available active sites and pores, the first cycle had the maximum adsorption due to the maximum available active sites and pores. The decreased adsorption observed in the other cycles is due to the inability to absorb U(VI) during regeneration, resulting in the blockage of some of the active sites.

4 Conclusion

In this study, medlar seeds were used as a raw material to produce activated carbon by H_3PO_4 impregnation followed by thermal activation. The resulting activated carbons were analyzed using SEM–EDX, FTIR, pH_{PZC}, and nitrogen adsorption–desorption techniques. The results obtained showed that the impregnation ratio and temperature of activation played a significant role in obtaining activated carbon with good surface properties. A maximum BET surface area of 1845.32 m^2/g was obtained with an H_3PO_4 impregnation ratio of 2:1 at 500 °C after 60 min. Batch uranium adsorption experiments identified the optimal conditions as a pH of 3.54, a uranium concentration of 100 mg/L, a contact time of 90 min, an adsorbent dose of 2 g/L, and particle sizes ranging from 0.125 to 0.20 nm. The adsorption isotherms aligned well with the Langmuir model ($R^2 > 0.99$), indicating a monolayer adsorption process with a maximum capacity of 52.08 mg/g. Kinetic analysis showed that the sorption followed a pseudo-second-order model and the rate-limiting step was chemical adsorption. Additionally, thermodynamic studies indicated that the adsorption of uranium on AC-500–2 is a spontaneous, exothermic, and favorable process.

Acknowledgements The authors thank all those who contributed to the realization of this work.

Author contribution Messaoud BENNEMLA: conceptualization, supervision, and writing original manuscript; Toufik SEMAOUNE: review and editing; Meriem CHABANE SARI: review and editing; Fatima HOUHOUNE: review and editing; Sihem KHEMAISSIA: methodology and resources; Mourad BELLALOUI: formal analysis; Hamana ADJEDAR: material preparation; Yasmina; HAMMACHE: formal analysis; Sihem OUATTAS: formal analysis.

Funding The present study was financially supported by Nuclear Research Center of Draria (Algiers). The authors are grateful to the Directorate General for Nuclear Research Center of Draria for financial support.

Declarations

Conflict of interest The authors declare no competing interests.

References

1. Kalin M, Wheeler WN, Meinrath G (2005) The removal of uranium from mining waste water using algal/microbial biomass. J Environ Radioact 78:151–177
2. Preetha CR, Gladis JM, Rao TP, Venkateswaran G (2006) Removal of toxic uranium from synthetic nuclear power reactor effluents using uranyl ion imprinted polymer particles. Environ Sci Technol 40:3070–3074
3. Xie Y, Chen C, Ren X, Wang X, Wang H, Wang X (2019) Emerging natural and tailored materials for uranium-contaminated water treatment and environmental remediation. Prog Mater Sci 103:180–234
4. Li LY, Li H, Lin MZ, Wen J, Hu S (2022) Effects of chain conformation on uranium adsorption performance of amidoxime adsorbents. Sep Purif Technol. https://doi.org/10.1016/j.seppur.2022.122777
5. Das A, Jana A, Das D, Biswas S, Sheshadri H, Rao MS (2023) Surfactant assisted APTES functionalization of graphene oxide intercalated layered double hydroxide (LDH) for uranium adsorption from alkaline leach liquor. J Clean Prod. https://doi.org/10.1016/j.jclepro.2023.136058
6. Brugge D, deLemos JL, Oldmixon B (2005) Exposure pathways and health effects associated with chemical and radiological toxicity of natural uranium: a review. Rev Environ Health 20:177–194
7. Sharma DA, Keesari T, Rishi MS, Thakur N, Pant D, Sangwan P, Sahoo BK, Kishore N (2020) Distribution and correlation of radon and uranium and associated hydrogeochemical processes in alluvial aquifers of northwest India. Environ Sci Pollut Res 27:38901–38915
8. Ahmad Z, Li Y, Yang J, Geng N, Fan Y, Gou X, Sun Q, Chen J (2022) A membrane supported bifunctional poly(amidoxime-ethyleneimine) network for enhanced uranium extraction from seawater and wastewater. J Hazard Mater. https://doi.org/10.1016/j.jhazmat.2021.127995
9. Xiong T, Li Q, Liao J, Zhang Y, Zhu W (2021) Highly enhanced adsorption performance to uranium (VI) by facile synthesized hydroxyapatite aerogel. J Hazard Mater. https://doi.org/10.1016/j.jhazmat.2021.127184
10. Appukuttan D, Rao AS, Apte SK (2006) Engineering of Deinococcus radiodurans R1 for bioprecipitation of uranium from dilute nuclear waste. Appl Environ Microbiol. https://doi.org/10.1128/AEM.01362-06
11. Astley V, Stana R (2014) There and back again 25 Again who did what in solvent extraction? A demonstrated & proven technology for uranium recovery from phosphoric acid. Procedia Engineering 83:270–278
12. Sarina S, Bo A, Liu D, Liu H, Yang D, Zhou C, Maes N, Komarneni S, Zhu H (2014) Separate or simultaneous removal of radioactive cations and anions from water by layered sodium vanadate-based sorbents. Chem Mater 26:4788–4795
13. Merceille A, Weinzaepfel E, Barre Y, Grandjean A (2012) The sorption behaviour of synthetic sodium nonatitanate and zeolite A for removing radioactive strontium from aqueous wastes. Sep Purif Technol 96:81–88
14. Ding DH, Lei ZF, Yang YN, Zhang ZY (2014) Efficiency of transition metal modified akadama clay on cesium removal from aqueous solutions. Chem Eng J 236:17–28
15. Hang T, Nash CA, Aleman SE (2013) Modeling ion-exchange processing with spherical resins for cesium removal. Sep Sci Technol 48:2090–2098
16. Torkabad MG, Keshtkar AR, Safdari SJ (2017) Comparison of polyethersulfone and polyamide nanofiltration membranes for uranium removal from aqueous solution. Prog Nucl Energy 94:93–100
17. Liu Y, Yuan L, Yuan Y, Lan J, Li Z, Feng Y, Zhao Y, Chai Z, Shi W (2012) A high efficient sorption of U(VI) from aqueous solution using amino-functionalized SBA-15. J Radioanal Nucl Chem 292:803–810
18. Xu M, Han X, Hua D (2017) Polyoxime-functionalized magnetic nanoparticles for uranium adsorption with high selectivity over vanadium. J Mater Chem 5:12278–12284
19. Houhoune F, Khemaissia S, Nibou D, Chegrouche S, Menacer S (2018) Kinetic study and sorption mechanism of uranium (VI) onto NaY zeolite. AIP Conf Proc 1994:070008. https://doi.org/10.1063/1.5048180
20. Tobilko V, Spasonova L, Kovalchuk I, Kornilovych B, Kholodko Y (2019) Adsorption of uranium (VI) from aqueous solutions by amino-functionalized clay minerals. Colloids and Interfaces. https://doi.org/10.3390/colloids3010041
21. Kütahyali C, Eral M (2004) Selective adsorption of uranium from aqueous solutions using activated carbon prepared from charcoal by chemical activation. Separ Purif Technol 40:109–114
22. Liu X, Ma C, Wen Y, Chen X, Zhao X, Tang T, Holze R, Mijowska E (2021) Highly efficient conversion of waste plastic into thin carbon nanosheets for superior capacitive energy storage. Carbon. https://doi.org/10.1016/j.carbon.2020.09.057
23. Wu Y, Luo H, Wang H, Wang C, Zhang J, Zhang Z (2013) Adsorption of hexavalent chromium from aqueous solutions by graphene modified with cetyltrimethylammonium bromide. J Colloid Interface Sci 394:183–191
24. Antero RVP, Alves ACF, Sales PTF, Oliveira SB, Ojala SA, Brum SS (2019) A new approach to obtain mesoporous-activated carbon via hydrothermal carbonization of Brazilian Cerrado biomass combined with physical activation for bisphenol-A removal. Chem Eng Commun 206:1498–1514. https://doi.org/10.1080/00986445.2019.1601625
25. Efeovbokhan VE, Alagbe EE, Odika B, Babalola R, Oladimeji TE, Abatan OG, Yusuf EO (2019) Preparation and characterization of activated carbon from plantain peel and coconut shell using biological activators. J Phys: Con Series 1378:032035. https://doi.org/10.1088/1742-6596/1378/3/032035
26. Jain A, Balasubramanian R, Srinivasan MP (2016) Hydrothermal conversion of biomass waste to activated carbon with high porosity: a review. Chem Eng J 283:789–805. https://doi.org/10.1016/j.cej.2015.08.014
27. Yahya MA, Al-Qodah Z, Ngah CZ (2015) Agricultural bio-waste materials as potential sustainable precursors used for activated carbon production: a review. Renew Sustain Energy Rev 46:218235
28. Somyanonthanakun W, Ahmed R, Krongtong V, Thongmee S (2023) Studies on the adsorption of Pb (II) from aqueous solutions using sugarcane bagasse-based modified activated carbon with nitric acid: kinetic, isotherm and desorption. Chem Phys Impact. https://doi.org/10.1016/j.chphi.2023.100181
29. Zhang X, Wu S, Liu Y, Wang Z, Zhang H, Xiao R (2023) Removal of Cr (VI) from aqueous solution by rice-husk-based activated carbon prepared by dual-mode heating method. Carbon Resour Conver 6:76–84

30. Miao Q, Tang Y, Xu J, Liu X, Xiao L, Chen Q (2013) Activated carbon prepared from soybean straw for phenol adsorption. J Taiwan Inst Chem Eng 44:458–465. https://doi.org/10.1016/j.jtice.2012.12.006
31. La biodiversité cultivée pour adapter l'agriculture régionale au changement climatique, Néflier du Japon. DiversiGO 2021–2023. https://www.bio-provence.org/IMG/pdf/fiche_neflier-2.pdf
32. Gruz J, Ayaz FA, Torun H, Strnad M (2011) Phenolic acid content and radical scavenging activity of extracts from medlar (Mespilus germanica L) fruit at different stages of ripening. Food Chem 124:271–277. https://doi.org/10.1016/j.foodchem.2010.06.030
33. Hamoda MF (2017) Management of discarded organic produce from supermarkets and hypermarkets. Int J Environ Waste Manag 20:264–282. https://doi.org/10.1504/IJEWM.2017.087168
34. Cerovic LJS, Milonjic SK, Todorovic MB, Trtanj MI, pogozhev YS, Blagoveschenskii Y, Levashov EA, (2006) Point of zero charge of different carbides. Colsurfs Physicochem Eng Aspects. https://doi.org/10.1016/j.colsurfa.2006.10.012
35. Thommes M, Kaneko K, Neimark AV, Olivier JP, Rodriguez-Reinoso F, Rouquerol J, Sing KSW (2015) Physisorption of gases, with special reference to the evaluation of surface area and pore size distribution (IUPAC Technical Report). Pure Appl Chem 87:1051–1069
36. Xie L, Meng Y, Wang Q, Zhang G, Xie H, Zhou G (2022) Zanthoxylum bungeanum branches activated carbons with rich micropore structure prepared by low temperature H_3PO_4 hydrothermal pretreatment method for toluene adsorption. Diam Relat Mater. https://doi.org/10.1016/j.diamond.2022.109474
37. Cychosz KA, Guillet-Nicolas R, García-Martínez J, Thommes M (2017) Recent advances in the textural characterization of hierarchically structured nanoporous materials. Chem Soc Rev 46:310–323
38. Chandra TC, Mirna MM, Sunarso J, Sudaryanto Y, Ismadji S (2009) Activated carbon from durian shell: preparation and characterization. J Taiwan Inst Chem Eng 40:457–462
39. Gao Q, Yang J, Xiang H, Ni L, Hou Y, He Y, Hu Z, Feng W, Liu Z (2021) Nitrogen self-doped activated carbons with narrow pore size distribution from bamboo shoot shells. Colloids Surf, A. https://doi.org/10.1016/j.colsurfa.2021.127408
40. Lim WC, Srinivasakannan C, Al Shoaibi A (2015) Cleaner production of porous carbon from palm shells through recovery and reuse of phosphoric acid. J Clean Prod 102:501–511
41. Al Bahri M, Calvo L, Gilarranz MA, Rodriguez JJ (2012) Activated carbon from grape seeds upon chemical activation with phosphoric acid: application to the adsorption of diuron from water. Chem Eng J 203:348–356. https://doi.org/10.1016/j.cej.2012.07.053
42. Tham YJ, Latif PA, Abdullah AM, Shamala-Devi A, Taufiq-Yap YH (2011) Performances of toluene removal by activated carbon derived from durian shell. Bioresour Technol 102:724–728
43. Demiral I, Samdan CA (2016) Preparation and characterisation of activated carbon from pumpkin seed shell using H3PO4, Anadolu Univ. J Sci Technol A-Appl Sci Eng 17:125138
44. Lee CL, H'ng PS, Paridah MT, Chin KL, Rashid U, Maminski M, Go WZ, Nazrin RAR, Rosli SNA, Khoo PS (2018) Production of bioadsorbent from phosphoric acid pretreated palm kernel shell and coconut shell by two-stage continuous physical activation via N_2 and air. R Soc Open Sci 5:180775
45. Geczo A, Giannakoudakis DA, Triantafyllidis K, Elshaer MR, Rodríguez-Aguado E, Bashkova S (2021) Mechanistic insights into acetaminophen removal on cashew nut shell biomass-derived activated carbons. Environ Sci Pollut Control Ser 28:58969–58982. https://doi.org/10.1007/s11356-019-07562-0
46. Haghbin MR, Shahrak MN (2021) Process conditions optimization for the fabrication of highly porous activated carbon from date palm bark wastes for removing pollutants from water. Powder Technol 377:890899
47. Neme I, Gonfa G, Masi C (2022) Preparation and characterization of activated carbon from castor seed hull by chemical activation with H_3PO_4. Results in Materials 5:100304. https://doi.org/10.1016/j.rinma.2022.100304
48. Lopez FA, Centeno TA, García-Diaz I, Alguacil FJ (2013) Textural and fuel characteristics of the chars produced by the pyrolysis of waste wood, and the properties of activated carbons prepared from them. J Anal Appl Pyrol 104:551–558
49. Mazlan MAF, Uemura Y, Yusup S, Elhassan F, Uddin A, Hiwada A, Demiya M (2016) Activated carbon from rubber wood sawdust by carbon dioxide activation. Procedia Eng 148:530537. https://doi.org/10.1016/j.proeng.2016.06.549
50. Han Q, Wang J, Goodman BA, Xie J, Liu Z (2020) High adsorption of methylene blue by activated carbon prepared from phosphoric acid treated eucalyptus residue. Powder Technol 366:239–248
51. Kumar A, Jena HM (2016) Preparation and characterization of high surface area activated carbon from Fox nut (Euryale ferox) shell by chemical activation with H_3PO_4. Results in Physics 6:651–658
52. Trinh TK, Tsubota T, Takahashi S, Mai NT, Nguyen MN, Nguyen NH (2020) Carbonization and H_3PO_4 activation of fern Dicranopteris linearis and electrochemical properties for electric double layer capacitor electrode. Sci Rep 10:19974–19974
53. Quach NKN, Yang WD, Chung ZJ, Tran HL (2017) The influence of the activation temperature on the structural properties of the activated carbon xerogels and their electrochemical performance. Adv Mater Sci Eng. https://doi.org/10.1155/2017/8308612
54. Caillat S, Vakkilainen E (2013) 9 -Large-scale Biomass Combustion Plants: an Overview. Biomass combustion science, technology and engineering. https://doi.org/10.1533/9780857097439.3.189
55. Queiroz LS, de Souza LKC, Thomaz KTC, Leite Lima ET, da Rocha Filho GN, do Nascimento LAS, de OliveiraPires LH, Faial KdCF, da Costa CEF (2020) Activated carbon obtained from amazonian biomass tailings (acai seed): modification, characterization, and use for removal of metal ions from water. J Environ Manag 270:110868. https://doi.org/10.1016/j.jenvman.2020.110868
56. Kahvecioğlu K, Teğin İ, Yavuz Ö, Saka C (2023) Phosphorus and oxygen co-doped carbon particles based on almond shells with hydrothermal and microwave irradiation process for adsorption of lead (II) and cadmium (II). Environ Sci Pollut Res 30:37946–37960. https://doi.org/10.1007/s11356-022-24968-5
57. Yang J, Qiu K (2010) Preparation of activated carbons from walnut shells via vacuum chemical activation and their application for methylene blue removal. Chem Eng J. https://doi.org/10.1016/j.cej.2010.09.019
58. Zhang L, Tan J, Xing G et al (2021) Cotton stalk-derived hydrothermal carbon for methylene blue dye removal: investigation of the raw material plant tissues. Bioresour Bioprocess 8:1–11. https:// doi. org/ 10. 1186/ S40643- 021- 00364–8/FIGUR ES/7
59. Liu Y, Wang L, Wang X, Jing F, Chang R, Chen J (2020) Oxidative ageing of biochar and hydrochar alleviating competitive sorption of Cd(II) and Cu(II). Sci Total Environ 725:138419. https://doi.org/10.1016/j.scitotenv.2020.138419
60. Xu J, Chen L, Qu H, Jiao Y, Xie J, Xing G (2014) Preparation and characterization of activated carbon from reedy grass leaves by chemical activation with H_3PO_4. Appl Surf Sci 320:674–680. https://doi.org/10.1016/j.apsusc.2014.08.178
61. Politou AS, Morterra C, Low MJD (1990) Infrared studies of carbons XII the formation of chars from a polycarbonate. Carbon 28:529–538

62. Öc S, Teğin İ, Yabalak E, Saka C (2023) Facile modification strategies on hydrochar-based carbon particles with hydrothermal carbonization from green pistachio hulls for the removal of cadmium ions from aqueous solutions. Biomass Conver Biorein. https://doi.org/10.1007/s13399-023-05242-1
63. Luo Y, Li D, Chen Y, Sun X, Cao Q, Liu X (2019) The performance of phosphoric acid in the preparation of activated carbon-containing phosphorus species from rice husk residue. J Mater Sci 54:5008–5021. https://doi.org/10.1007/s10853-018-03220-x
64. Yorgun S, Yıldız D (2015) Preparation and characterization of activated carbons from Paulownia wood by chemical activation with H_3PO_4. J Taiwan Inst Chem Eng 53:122–131. https://doi.org/10.1016/j.jtice.2015.02.032
65. Suganya S, Kumar PS (2018) Kinetic and thermodynamic analysis for the redemption of effluents containing Solochrome Black T onto powdered activated carbon: a validation of new solid-liquid phase equilibrium model. J Mol Liq 259:88–101
66. Teğin İ, Öc S, Saka C (2024) Facile phosphorus and oxygen heteroatom functionalization of biochar based on biomass prepared by microwave pyrolysis for adsorption process of cadmium in aqueous solution. Biomass Conver Biorein. https://doi.org/10.1007/s13399-024-05644-9
67. Puziy AM, Poddubnaya OI, Martínez-Alonso A, Suárez-García F, Tascón JMD (2002) Synthetic carbons activated with phosphoric - acid I. Surface chemistry and ion binding properties. Carbon N Y 40:1493–1505. https://doi.org/10.1016/S0008-6223(01)00317-7
68. Niloufar Nekouei M, Afsaneh S (2019) A novel environmental-friendly nanobiocomposite synthesis by EDTA and chitosan functionalized magnetic graphene oxide for high removal of Rhodamine B: adsorption mechanism and separation property. Chemosphere 218:715–725
69. Sutirman ZA, Sanagi MM, Abd Karim KJ, Wan Ibrahim WA (2016) Preparation of methacrylamide-functionalized crosslinked chitosan by free radical polymerization for the removal of lead ions. Carbohydr Polym 151:1091–1099
70. Zhou L, Ouyang J, Liu Z, Huang G, Wang Y, Li Z, Adesina AA (2019) Highly efficient sorption of U(VI) from aqueous solution using amino/amine-functionalized magnetic mesoporous silica nanospheres. J Radioanal Nucl Chem 319:987–995
71. Tuzen M, Sari A, Saleh T (2020) Synthesis, characterization and evaluation of carbon nanofiber modified-polymer for ultra-removal of thorium ions from aquatic media. Chem Eng Res Des 163:76–84
72. Zheng B, Liao J, Ding L, Zhang Y, Zhu W (2021) High efficiency adsorption of uranium in solution with magnesium oxide embedded horse manure-derived biochar. J Environ Chem Eng. https://doi.org/10.1016/j.jece.2021.106897
73. Erdem E, Karapinar N, Donat R (2004) The removal of heavy metal cations by natural zeolites. J Colloid Interface Sci 280:309–314
74. Foroutan R, Peighambardoust SJ, Esvandi Z, Khatooni H, Ramavandi B (2021) Evaluation of two cationic dyes removal from aqueous environments using CNT/MgO/$CuFe_2O_4$ magnetic composite powder: a comparative study. J Environ Chem Eng 9:104752
75. Bilici Baskan M, Pala A (2011) Removal of arsenic from drinking water using modified natural zeolite. Desalination. https://doi.org/10.1016/j.desal.2011.08.015
76. Zhao L, Wang S, Zhuang H, Lu B, Sun L, Wang G, Qiu J (2022) Facile synthesis of low-cost $MnPO_4$ with hollow grape-like clusters for rapid removal uranium from wastewater. J Hazard Mater. https://doi.org/10.1016/j.jhazmat.2022.128894
77. Gurav R, Bhatia SK, Choi T-R, Kim HJ, Choi Y-K, Lee H-J, Ham S, Cho JY, Kim SH, Lee SH, Yun J, Yang Y-H (2022) Adsorptive removal of synthetic plastic components bisphenol-A and solvent black-3 dye from single and binary solutions using pristine pinecone biochar. Chemosphere. https://doi.org/10.1016/j.chemosphere.2022.134034
78. Kumar M, Singh AK, Sikandar M (2018) Study of sorption and desorption of Cd (II) from aqueous solution using isolated green algae Chlorella vulgaris. Appl Water Sci 8:1–11. https://doi.org/10.1007/s13201-018-0871-y
79. Fu L, Li J, Wang G, Luan Y, Dai W (2021) Adsorption behavior of organic pollutants on microplastics. Ecotox Environ Safe. https://doi.org/10.1016/j.ecoenv.2021.112207
80. Wang J, Guo X (2020) Adsorption kinetic models: physical meanings, applications, and solving methods. J Hazard Mater. https://doi.org/10.1016/j.jhazmat.2020.122156
81. Han XW, Wang YQ, Cao XH, Dai Y, Liu YH, Dong ZM, Zhang ZB, Liu YH (2019) Adsorptive performance of ship-type nanocage polyoxometalates for U(VI) in aqueous solution. Appl Surf Sci 481:1035–1040
82. Yan J, Li K (2021) A magnetically recyclable polyampholyte hydrogel adsorbent functionalized with β-cyclodextrin and graphene oxide for cationic/anionic dyes and heavy metal ion wastewater remediation. Sep Purif Technol 277:119469
83. Aslani CK, Amik O (2021) Active carbon/PAN composite adsorbent for uranium removal: modeling adsorption isotherm data, thermodynamic and kinetic studies. Appl Radiat Isot 168:109474. https://doi.org/10.1016/j.apradiso.2020.109474
84. Xiao-teng Z, Dong-mei J, Yi-qun X, Jun-chang C, Shuai H, Liang-shu X (2019) Adsorption of uranium (VI) from aqueous solution by modified rice stem. J Chem. https://doi.org/10.1155/2019/6409504
85. Kütahyalı C, Eral M (2010) Sorption studies of uranium and thorium on activated carbon prepared from olive stones: kinetic and thermodynamic aspects. J Nucl Mater 396:251–256. https://doi.org/10.1016/j.jnucmat.2009.11.018
86. Liu C, Fu Y, Li Y, Liu S, Zhou Y, Liu D, Fu C, Ye L (2023) $UO2^{2+}$ capture using amidoxime grafting low-cost activated carbon (AO-AC) from solution: adsorption kinetic, isotherms and interaction mechanism. Inorg Chim Acta 544:121226. https://doi.org/10.1016/j.ica.2022.121226
87. Wu L, Caoc Y, Li Z, Hu L, Zhang Z, Yu Q (2020) Preparation of areca residue activated carbon composite and its adsorption performance for uranium (VI) in wastewater. Desalin Water Treat 182:144–154. https://doi.org/10.5004/dwt.2020.25136
88. Sen K, Mishra D, Debnath P, Mondal A, Mondal NK (2021) Adsorption of uranium (VI) from groundwater by silicon containing biochar supported iron oxide nanoparticle. Bioresour Technol Rep 14 https://doi.org/10.1016/j.biteb.2021.100659
89. Teğin İ, Batur MŞ, Yavuz Ö, Saka C (2023) Removal of Cu (II), Pb (II) and Cd (II) metal ions with modified clay composite: kinetics, isotherms and thermodynamics studies. Int J Environ Sci Technol 20:1341–1356. https://doi.org/10.1007/s13762-022-04028-8